

## Article

# Coordinating Etching Inspired Synthesis of Fe(OH)<sub>3</sub> Nanocages as Mimetic Peroxidase for Fluorescent and Colorimetric Self-Tuning Detection of Ochratoxin A

Hongshuai Zhu <sup>1,2,†</sup>, Bingfeng Wang <sup>2,†</sup>  and Yingju Liu <sup>2,\*</sup><sup>1</sup> College of Food Science and Technology, Henan Agricultural University, Zhengzhou 450003, China<sup>2</sup> Key Laboratory for Biobased Materials and Energy of Ministry of Education, College of Materials and Energy, South China Agricultural University, Guangzhou 510642, China

\* Correspondence: yingjuliu@scau.edu.cn; Tel.: +86-20-85280319; Fax: +86-20-85285026

† These authors contributed equally to this work.

**Abstract:** The development of multifunctional biomimetic nanozymes with high catalytic activity and sensitive response is rapidly advancing. The hollow nanostructures, including metal hydroxides, metal-organic frameworks, and metallic oxides, possess excellent loading capacity and a high surface area-to-mass ratio. This characteristic allows for the exposure of more active sites and reaction channels, resulting in enhanced catalytic activity of nanozymes. In this work, based on the coordinating etching principle, a facile template-assisted strategy for synthesizing Fe(OH)<sub>3</sub> nanocages by using Cu<sub>2</sub>O nanocubes as the precursors was proposed. The unique three-dimensional structure of Fe(OH)<sub>3</sub> nanocages endows it with excellent catalytic activity. Herein, in the light of Fe(OH)<sub>3</sub>-induced biomimetic nanozyme catalyzed reactions, a self-tuning dual-mode fluorescence and colorimetric immunoassay was successfully constructed for ochratoxin A (OTA) detection. For the colorimetric signal, 2,2'-azino-bis (3-ethylbenzothiazoline-6-sulfonic acid) diammonium salt (ABTS) can be oxidized by Fe(OH)<sub>3</sub> nanocages to form a color response that can be preliminarily identified by the human eye. For the fluorescence signal, the fluorescence intensity of 4-chloro-1-naphthol (4-CN) can be quantitatively quenched by the valence transition of Ferric ion in Fe(OH)<sub>3</sub> nanocages. Due to the significant self-calibration, the performance of the self-tuning strategy for OTA detection was substantially enhanced. Under the optimized conditions, the developed dual-mode platform accomplishes a wide range of 1 ng/L to 5 µg/L with a detection limit of 0.68 ng/L (S/N = 3). This work not only develops a facile strategy for the synthesis of highly active peroxidase-like nanozyme but also achieves promising sensing platform for OTA detection in actual samples.

**Keywords:** biomimetic nanozymes; coordinating etching; Fe(OH)<sub>3</sub> nanocages; dual-mode fluorescence and colorimetric immunoassay; ochratoxin A detection



**Citation:** Zhu, H.; Wang, B.; Liu, Y. Coordinating Etching Inspired Synthesis of Fe(OH)<sub>3</sub> Nanocages as Mimetic Peroxidase for Fluorescent and Colorimetric Self-Tuning Detection of Ochratoxin A. *Biosensors* **2023**, *13*, 665. <https://doi.org/10.3390/bios13060665>

Received: 27 April 2023

Revised: 9 June 2023

Accepted: 15 June 2023

Published: 19 June 2023



**Copyright:** © 2023 by the authors. Licensee MDPI, Basel, Switzerland. This article is an open access article distributed under the terms and conditions of the Creative Commons Attribution (CC BY) license (<https://creativecommons.org/licenses/by/4.0/>).

## 1. Introduction

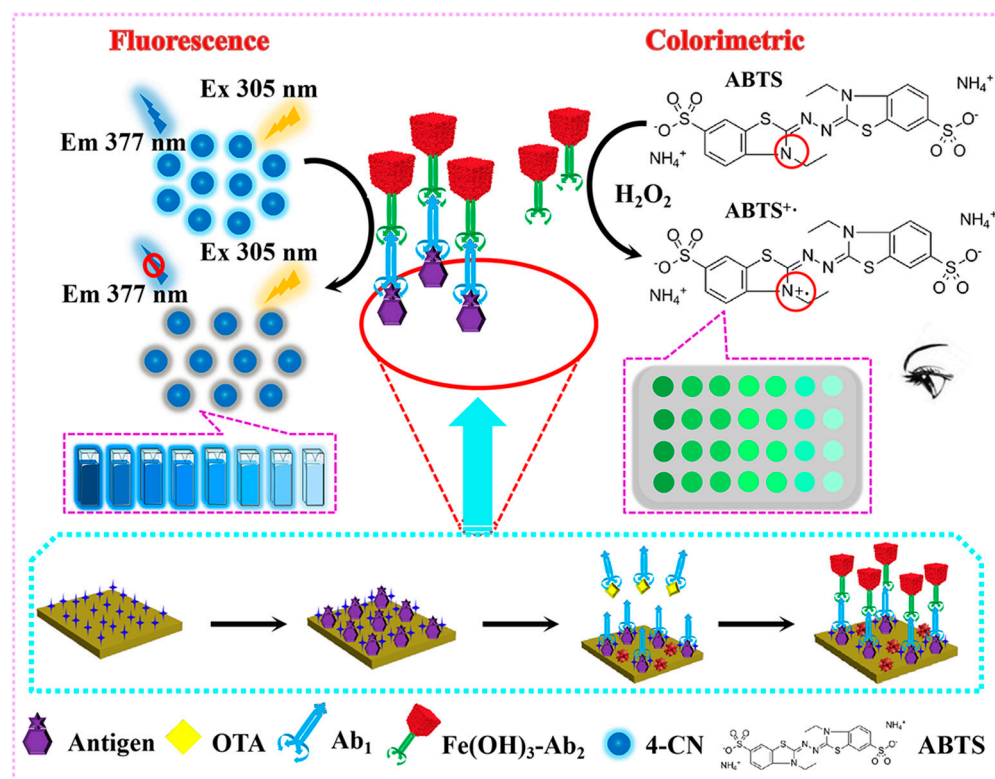
The colorimetric immunosensor has been supposed as a powerful technique to detect contaminants because of its inherent strength, such as simplicity of detection, low cost, and practicality [1–3]. Especially, this strategy can be recognized by human eyes without any sophisticated and expensive equipment [4]. For example, He et al. designed an ultra-sensitive visual method based on enzyme-induced gold nanoparticle aggregation to investigate the activity of alkaline phosphatase [5]. Wang et al. developed an online colorimetric acetone sensor by the specific reaction between hydroxylamine sulfate and acetone [6]. Mustafa proposed a highly specific enzyme-induced paper biosensor, which can predict fish freshness by monitoring the enzymatic conversion of hypoxanthine [7]. Moon et al. reported a colorimetric viral determination strategy in the light of the inter-spaced palindromic repeats (CRISPR)/Cas9 endonuclease dead system, which can successfully identify pH1N1/H275Y, pH1N1, and SARS-CoV-2 viruses through visualization [8]. Since

the detection results can be judged visually without complex equipment, the colorimetric immunosensor has been used for on-site and portable detection [9–11]. Nevertheless, unsatisfactory sensitivity and accuracy severely hampers its further development and wide application in practical measurement [12,13]. Consequently, in order to enhance the detection selectivity and sensitivity, dual-mode immunosensor has been proposed recently [14–17]. In light of the chromogenic properties of oxidized *p*-phenylenediamine and its inner filter effect with organic silicon nanodots, Li et al. established a dual-mode fluorescent and colorimetric sensor to detect glucose in serum [18]. By employing giant Au vesicles as an intelligent probe, Guo et al. proposed a facile and efficient surface-enhanced Raman scattering and colorimetric dual-mode immunoassay for ultra-sensitive detection of *Vibrio parahaemolyticus* [19]. Notwithstanding, the dual-mode immunosensor can generate two different response signals and avoid false negative and positive results. Nevertheless, the two signals only respond linearly to the target concentration, and there is no correlation between the two detection results. Hence, in this work, according to the Pearson correlation analysis, the dynamic response relationship between two signals in a dual-mode immunosensor was investigated. Eventually, to a certain degree, the proposed strategy can eliminate the disturbance of environmental factors and enhance the sensitivity for trace analysis.

The performance of the immunosensor was basically decided by the catalytic ability of the enzyme. To date, the development of natural enzymes has been greatly restricted due to the high cost and poor environmental tolerance. Concurrently, with the rapid development of nano-materials in recent years, nanozymes have been supposed as a feasible substitute for natural enzyme because of its extraordinary merits including cost-effectiveness, easy preparation, mass-production, multiple functionalities, high stability, and durability [20–22]. Since the accidental discovery of Fe<sub>3</sub>O<sub>4</sub> nanoparticles with peroxidase mimetic activity in 2007 [23], nanozymes have been reported for various applications. For instance, Chen et al. synthesized Co<sub>3</sub>O<sub>4</sub>@Co-Fe double-shelled nanocages by employing ZIF-67 as a starting template and then developed a colorimetric strategy for screening acetylcholinesterase activity by the high peroxidase mimetic activity of Co<sub>3</sub>O<sub>4</sub>@Co-Fe [24]. Mu et al. reported catalase mimics-like Co<sub>3</sub>O<sub>4</sub> with different morphology for the determination of calcium ion [25]. Jin et al. prepared Si-doped CoO (Si-CoO) nanorods via hydrothermal strategy, which showed excellent peroxidase mimetic activity, to construct a colorimetric sensor for the detection of glutathione [26]. Commendably, in previous studies, there is an interesting finding that most of the nanozymes are concentrated in metal oxides [27], metals [28], metal organic framework (MOFs) [29], and carbons [30]. Few studies have investigated the application of metal hydroxides in the field of nanozyme catalysis [31]. Recently, 3D metal hydroxides have been demonstrated to exhibit promising catalytic activity due to their structural characteristics and tremendous catalytic active sites. Particularly, 3D hollow metal hydroxides with controllable morphology, size, and properties have received more attention.

In this study, based on the coordinating etching principle, a facile template-assisted strategy was proposed for synthesizing Fe(OH)<sub>3</sub> nanocages by using Cu<sub>2</sub>O nanocubes as the templates. Simultaneously, Fe(OH)<sub>3</sub> nanocages were discovered to exhibit excellent properties of mimetic peroxidase. Fe(OH)<sub>3</sub> nanocages were used to anchor the secondary antibody (Ab<sub>2</sub>) and then introduced into an immunosensor by an indirect immune competitive strategy. Thus, as in Scheme 1, a self-tuning dual-mode immunosensor was constructed by an Fe(OH)<sub>3</sub>-mediated Fenton-like reaction. Meanwhile, ochratoxin A (OTA), the most widely distributed ochratoxins, was used as the target analyte to demonstrate the performance of the developed immunosensor [32,33]. After the specific immune reaction, the immobilized Fe(OH)<sub>3</sub>@Ab<sub>2</sub> in the 96-microplate can efficiently change the emission peak at 377 nm of 4-chloro-1-naphthol (4-CN) for the fluorescence signal, while, the non-immune bound Fe(OH)<sub>3</sub>@Ab<sub>2</sub> can be used to catalyze the chromogenic substrate of 2,2'-azino-bis(3-ethylbenzothiazoline-6-sulfonic acid) diammonium salt (ABTS) with the assistance of H<sub>2</sub>O<sub>2</sub> for the colorimetric signal. Consequently, the concentrations of OTA can be intuitively

and conveniently identified. Ultimately, the fluorescence and colorimetric signals showed a direct negative correlation, which realized the self-calibration of the dual-mode sensor and greatly enhanced its accuracy and reliability.



**Scheme 1.** Schematic illustration of the self-tuning dual-mode immunosensor for OTA detection: fluorescence and colorimetry.

## 2. Experimental Section

Materials and instruments are detailed in the Supporting Information.

### 2.1. Synthesis of $\text{Fe}(\text{OH})_3$ Nanocages

$\text{Fe}(\text{OH})_3$  nanocages were obtained according to Figure 1A. After  $\text{Cu}_2\text{O}$  templates were prepared according to the earlier research [34],  $\text{Fe}(\text{OH})_3$  nanocages were synthesized by removing the  $\text{Cu}_2\text{O}$  cubic templates and precipitating  $\text{Fe}(\text{OH})_3$  simultaneously. Briefly, 1.665 g polyvinylpyrrolidone was dissolved in 50 mL water, then  $\text{FeCl}_2 \cdot 4\text{H}_2\text{O}$  (0.0105 g) and  $\text{Cu}_2\text{O}$  templates (0.025 g) were dispersed by stirring for 10 min, followed by adding  $\text{Na}_2\text{S}_2\text{O}_3$  (5 mL, 0.6 M) at uniform speed and reacting for another 30 min. After washing by water and ethanol, the final product was dispersed in 10 mL methanol. All processes were carried out at room temperature and pH 10.

### 2.2. Peroxidase Kinetics of the $\text{Fe}(\text{OH})_3$ Nanozyme

The kinetic parameters of the  $\text{Fe}(\text{OH})_3$  nanozyme were deduced by monitoring the adsorption of the mixture including the  $\text{Fe}(\text{OH})_3$  nanozyme,  $\text{H}_2\text{O}_2$ , and ABTS at 415 nm with the time. First, in HAc-NaAc buffer (0.2 M, pH = 4), a fixed concentration of the  $\text{Fe}(\text{OH})_3$  nanozyme (180  $\mu\text{M}$ ) and  $\text{H}_2\text{O}_2$  (4.84 mM) was employed to study the kinetic parameters of ABTS by changing its concentration from 0.48 to 3.87 mM. Subsequently, the concentration of  $\text{H}_2\text{O}_2$  was altered between 1.45 and 4.84 mM while unchanging that of ABTS (3.87 mM). Then, the kinetic constants were obtained by using the Lineweaver–Burk plot from the Michaelis–Menten equation, as below:

$$\frac{1}{V} = \left( \frac{1}{[S]} \right) \left( \frac{K_m}{V_{max}} \right) + \frac{1}{V_{max}}$$

where  $V$  is the initial velocity and  $[S]$  is the ABTS or  $H_2O_2$  concentration. In addition,  $K_m$  and  $V_{max}$  are the Michaelis constant and the maximal reaction velocity, which can indicate the affinity between the  $Fe(OH)_3$  nanozyme and the substrate (ABTS or  $H_2O_2$ ).

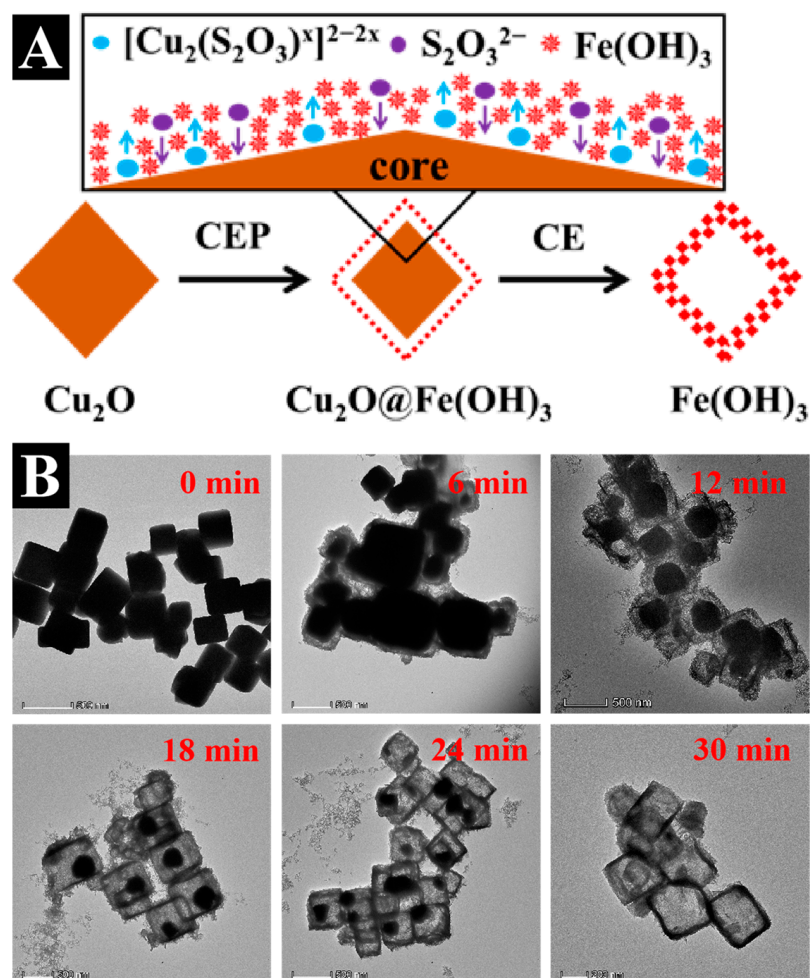


**Figure 1.** (A) Schematic diagram of  $Fe(OH)_3$  nanocages by the coordinating etching principle, CEP, coordinating etching and precipitating; CE, coordinating etching. (B) TEM images of the time-dependence of  $Fe(OH)_3$  nanocages for different times.

Next, the catalytic performance of the  $Fe(OH)_3$  nanozyme was further explored by theoretical calculation. The structure of small molecules involved in the decomposition of  $H_2O_2$  were constructed by Gviewer 5.0, then geometry optimization was carried with the density functional theory (DFT) at M06-2X/CC-PVDZ basis set level [35,36]. There are two possible configurations of the d orbital electron in the ferric atom including high spin and low spin. It can be confirmed by calculation that the high spin configuration was tested to be more stable, so all the following calculations were set as high spin. According to the earlier report [37], the  $H_2O_2$  decomposition mechanism was explored by calculating the energy change and transition state, so the difficulty degree of catalytic reaction was further demonstrated. As for the catalysis of the ferric ion on  $H_2O_2$ , the key step is the OH and  $O_2^-$  radicals generated by the  $H_2O_2$  with the valence transition of the ferrous ion in  $Fe(OH)_3$  nanocages. However, geometries of amorphous ferric oxide in the solvent are uncertain, so the numbers of water linked at the active position are uncertain, and several ferrous clusters may be connected together. Hence, a creative model was built, replacing the water molecule by dummy atoms. All calculations were finished with Gaussian 16 program. Data and figures including orbitals energy, orbital population, and ultraviolet frequencies were extracted by MultiWFN 3.7.

### 2.3. Preparation of $\text{Fe}(\text{OH})_3@Ab_2$

Firstly,  $\text{Fe}(\text{OH})_3$  nanocages were aminated by employing 7.2 mL of the above solution and 0.2 mL 3-aminopropyl trimethoxysilane (APTMS) to ethanol (35.6 mL), followed by stirring gently at 30 °C for 24 h, centrifuging and re-dispersing in Tris-HAc solution (10 mM). Next, the mixture (2 mL) was ultrasonicated at a low temperature for 20 min, and 4  $\mu\text{L}$   $Ab_2$  (1 mg/mL) was injected and stirred gently at 4 °C for 24 h. Finally, the mixture was centrifuged at a low temperature and re-dispersed in PBS (2 mL) for further use. Therefore, based on the covalent binding between amino groups of  $\text{Fe}(\text{OH})_3$  nanozyme and carboxyl groups of the second antibody ( $Ab_2$ ), the  $\text{Fe}(\text{OH})_3@Ab_2$  immune complex was synthesized for target recognition and signal output.

### 2.4. The Construction of the Self-Tuning Immunoassay

Briefly, 50  $\mu\text{L}$  dopamine (1 mg/mL) was injected into the micro-plate and incubated at 37 °C for 30 min. After drying, the OTA antigen (30  $\mu\text{L}$ , 10  $\mu\text{g}/\text{mL}$ ) was injected and held at 37 °C for 2 h. Consequently, in order to seal up the rest of the unspecific sites, 30  $\mu\text{L}$  blocking mixture was added. Subsequently, the solution (30  $\mu\text{L}$ ) containing various concentrations of OTA and a fixed amount of antibody ( $Ab_1$ , 5  $\mu\text{g}/\text{mL}$ ) was added to each well, then kept at 37 °C for 60 min (each well was washed by PBST and dried with  $\text{N}_2$  after each step). Next, the  $\text{Fe}(\text{OH})_3@Ab_2$  solution (30  $\mu\text{L}$ ) was injected and kept at 37 °C for 60 min, and the unconjugated solution was collected. Finally, 20  $\mu\text{L}$  PBST was injected into each well to wash the microplate, which was collected and mixed with the above unconjugated solution.

Afterwards, for the fluorescence signal, after the sandwich immunoreaction, 150  $\mu\text{L}$  of 4-CN (0.4 mM) was transferred into the above microplate and reacted for 4 min. The fluorescent intensity of the mixture was monitored by a fluorescence spectrometer. Additionally, for the colorimetric signal, 30  $\mu\text{L}$  unconjugated mixed solution, 200  $\mu\text{L}$  of pH 4.5 HAc-NaAc buffer (0.2 M), 30  $\mu\text{L}$  ABTS (30 mM), and 50  $\mu\text{L}$   $\text{H}_2\text{O}_2$  (35 mM) were sequentially added in a new 96-well plate. After reacting at 25 °C for 3 min, the solution color was changed into green and photographed by an iPhone 12, while the absorption intensity was monitored by a UV-vis spectrophotometer.

## 3. Results and Discussion

### 3.1. Characterization of $\text{Fe}(\text{OH})_3$ Nanocages

According to the coordinating etching principle, a facile strategy was developed to synthesize  $\text{Fe}(\text{OH})_3$  nanocages by carefully controlling the precipitation rate of  $\text{Fe}(\text{OH})_3$  and the coordinating etching rate towards the sacrificial templates of  $\text{Cu}_2\text{O}$  (Figure 1A) [38]. The reaction between  $\text{Fe}^{2+}$  and  $\text{Cu}_2\text{O}$  follows Pearson's hard and soft acid-base principle, where soft acids prefer to form stable complexes with soft bases, while hard Lewis acids prefer hard bases. Leveraging the soft acid properties of  $\text{Cu}^+$  within the  $\text{Cu}_2\text{O}$  templates, the coordinating etchant  $\text{S}_2\text{O}_3^{2-}$  was chosen. Initially,  $\text{S}_2\text{O}_3^{2-}$  formed soluble and stable  $[\text{Cu}_2(\text{S}_2\text{O}_3)_x]^{2-2x}$  complexes on the  $\text{Cu}_2\text{O}$  surface. Simultaneously, a significant amount of  $\text{OH}^-$  was generated from the interaction of  $\text{S}_2\text{O}_3^{2-}$  with water during the etching process. Consequently,  $\text{OH}^-$  and  $\text{Fe}^{2+}$  accumulated around  $\text{Cu}_2\text{O}$ , gradually forming a  $\text{Fe}(\text{OH})_2$  shell. Under the experimental conditions, the formed  $\text{Fe}(\text{OH})_2$  was oxidized to the more stable  $\text{Fe}(\text{OH})_3$ . This was evident from the maroon color observed in Figure S3. The size of the  $\text{Cu}_2\text{O}$  nanocubes decreases over time while retaining their cubic morphology, ultimately leading to the fabrication of nanocage structures.

To further verify these conclusions, transmission electron microscopy (TEM) was employed to demonstrate the whole etching process. As shown in Figure 1B, after 6 min of the etching reaction, the generated  $\text{Fe}(\text{OH})_3$  nanosheets adhered to  $\text{Cu}_2\text{O}$  nanocubes to form a stable film-like structure. The etching speed of  $\text{Cu}_2\text{O}$  nanocubes far exceeded the formation speed of  $\text{Fe}(\text{OH})_3$  nanosheets, so a cavity structure was clearly formed between  $\text{Cu}_2\text{O}$  and  $\text{Fe}(\text{OH})_3$  when the reaction time was prolonged to 12 min. Subsequently, with the extension of the etching time, it can be clearly observed that the  $\text{Cu}_2\text{O}$  cores

gradually decreased until it was completely etched, and the nanocages were successfully synthesized. In addition, from the formation process of nanocage structure, it can be found that the  $[\text{Cu}_2(\text{S}_2\text{O}_3)^x]^{2-2x}$  and  $\text{S}_2\text{O}_3^{2-}$  can easily flow in through the  $\text{Fe}(\text{OH})_3$  shells by inter-particle interstitials, which may be due to the well-distributed pore size of formed  $\text{Fe}(\text{OH})_3$  (12.27 nm, Figure 2C). In addition, the uniform porous structure of  $\text{Fe}(\text{OH})_3$  nanocages can increase the friction of its contact surface, which prolongs the contact time between  $\text{Fe}(\text{OH})_3$  and the substrate. The interesting nature of  $\text{Fe}(\text{OH})_3$  nanocages can enormously accelerate the passage of reactive substrates and products into or out of the channels, and simultaneously provide more accessible active sites. Additionally, as shown in Figure 2B of the  $\text{N}_2$  absorption–desorption curve, the Brunauer–Emmett–Teller (BET) surface area exhibited obvious increase from  $2 \text{ m}^2/\text{g}$  for  $\text{Cu}_2\text{O}$  (Figure S1) to  $134 \text{ m}^2/\text{g}$  for  $\text{Fe}(\text{OH})_3$  nanocages. Consequently,  $\text{Fe}(\text{OH})_3$  nanocages can provide more catalytic active sites and increase the rate of substrate diffusion [26]. Thus, the nanozyme activity and catalytic efficiency were substantially enhanced.

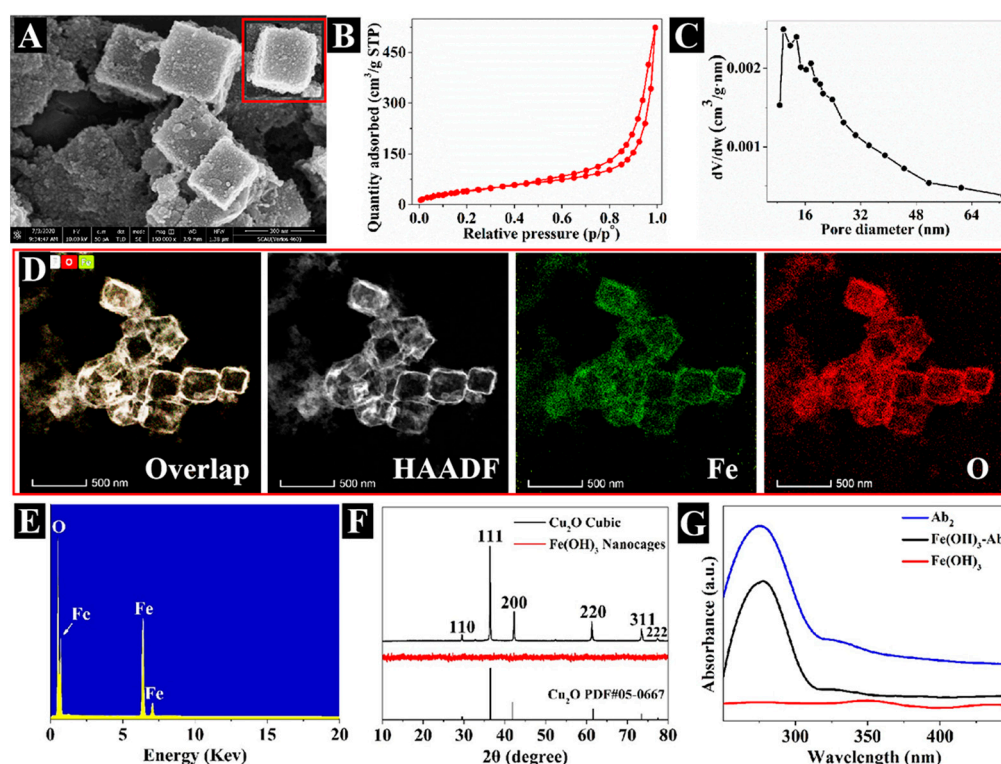


**Figure 2.** (A) SEM, (B)  $\text{N}_2$  absorption–desorption isotherm, (C) pore size distribution, (D) elemental mappings, (E) EDS, and (F) XRD of  $\text{Fe}(\text{OH})_3$  nanocages. (G) UV–vis spectra of  $\text{Fe}(\text{OH})_3@Ab_2$ .

In order to further investigate the surface and internal structures of the generated  $\text{Fe}(\text{OH})_3$  nanocages, scanning electron microscopy (SEM) and TEM photographs of  $\text{Fe}(\text{OH})_3$  nanocages and  $\text{Cu}_2\text{O}$  precursors were analyzed. As depicted in Figure S2A, it can be observed that monodisperse  $\text{Cu}_2\text{O}$  exhibited smooth surface, uniform particle size, and stable tetragonal structure. When the etching process completed, the prepared  $\text{Fe}(\text{OH})_3$  nanocages formed a sheet-like saddle-backing surface (Figure 2A), but it still kept a complete tetragonal spatial structure. Such unique appearance may also be the main reason for the significant increase in the surface area-to-mass ratio of  $\text{Fe}(\text{OH})_3$ . In addition, it can provide a very convenient condition for the attachment of bio-molecules and the reaction of chromogenic substrates.

Furthermore, compared with  $\text{Cu}_2\text{O}$  (Figure S2D), the elemental mappings of  $\text{Fe}(\text{OH})_3$  (Figure 2D) revealed that O and Fe were well distributed on the  $\text{Fe}(\text{OH})_3$  surface. Additionally, from the energy dispersive spectrometry (EDS) of  $\text{Fe}(\text{OH})_3$  (Figure 2E) and  $\text{Cu}_2\text{O}$  (Figure S2C), it can be demonstrated that only O and Fe elements were distributed on

Fe(OH)<sub>3</sub> nanocages, which reflected that Cu<sub>2</sub>O nanocubes were completely etched. From the X-ray diffraction (XRD) spectrum in Figure 2F, the (220), (200), (110), (111), and (311) crystal planes of a cubic Cu<sub>2</sub>O can be found at 61.3°, 42.3°, 29.6°, 36.4°, and 73.5° (JCPDS 05-0667). However, when the Fe(OH)<sub>3</sub> nanocages were formed, it became amorphous material [26].

Finally, the chemical composition of Fe(OH)<sub>3</sub> nanocages was further investigated by X-ray photo-electron spectroscopy (XPS). From Figure 3A, it can be found that two binding energy bands at 284.4 eV and 529.9 eV attributed to C 1s and O 1s, respectively. Simultaneously, two adjacent peaks centered at 724.5–725.8 eV and 709.8–712.4 eV belonged to Fe 2p<sub>3/2</sub> and Fe 2p<sub>1/2</sub>, respectively [39]. Then, the oxidation states of Fe and O in Fe(OH)<sub>3</sub> nanocages were further studied. As shown in Figure 3B, based on the earlier work [38], the major peaks at 711.1 and 724.6 eV in the Fe 2p corresponded to Fe 2p<sub>3/2</sub> and 2p<sub>1/2</sub>, which may be Fe<sup>3+</sup> in Fe(OH)<sub>3</sub>. Additionally, the peaks at 716.4 and 731.8 eV corresponded to the satellite peaks. As depicted in Figure 3C of O 1s, the peak at 529.5 eV also reflects the existence of the high valence state of Fe<sup>3+</sup>. The major peak at 530.8 eV indicated the existence of hydroxyl ions, while the weakly adsorbed oxygen species can be found at the peak at 532.2 eV [38]. Thus, the results revealed that the final synthetic product should be Fe(OH)<sub>3</sub> nanocages.

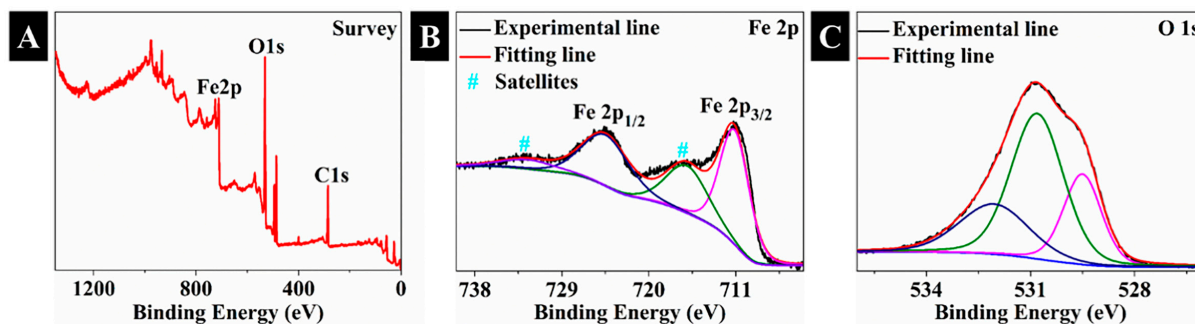


Figure 3. XPS survey (A), and the deconvolution of Fe 2p (B) and O 1s (C) of Fe(OH)<sub>3</sub> nanocages.

### 3.2. Catalytic Activity of Fe(OH)<sub>3</sub> Nanocages

The peroxidase-like behaviors of the Fe(OH)<sub>3</sub> nanozyme were studied by varying the concentrations of ABTS at a certain concentration of H<sub>2</sub>O<sub>2</sub> or varying concentrations of H<sub>2</sub>O<sub>2</sub> at a certain volume of ABTS. As seen from Figure 4A,B, the kinetic parameters of Fe(OH)<sub>3</sub> nanozyme and Cu<sub>2</sub>O were calculated by the Lineweaver–Burk plots, indicating that Fe(OH)<sub>3</sub> presented a lower  $K_m$  (0.7 mM) than that of Cu<sub>2</sub>O (0.77 mM) and horseradish peroxidase (HRP) (0.81 mM) [40]. Therefore, Fe(OH)<sub>3</sub> exhibited a stronger affinity for ABTS and H<sub>2</sub>O<sub>2</sub>.

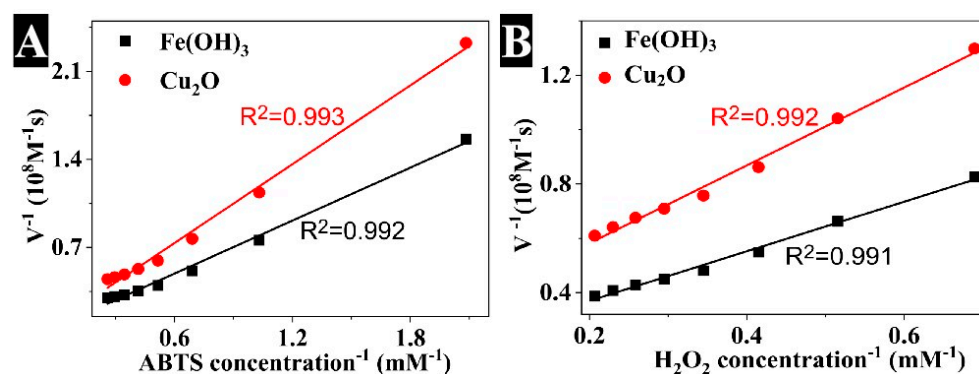
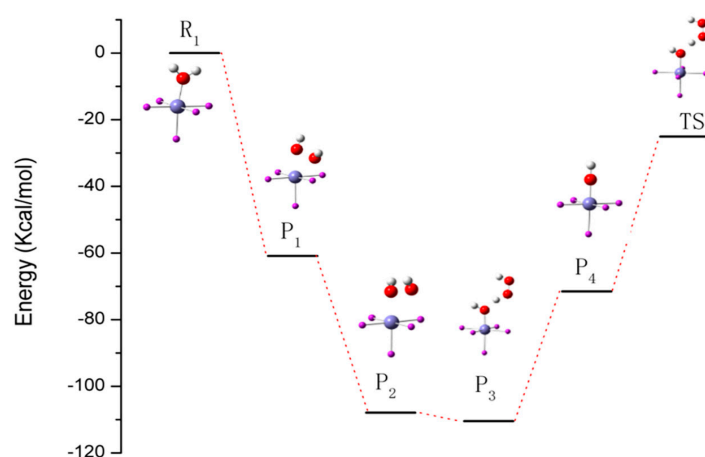


Figure 4. Lineweaver–Burk plots of Fe(OH)<sub>3</sub> nanocages and Cu<sub>2</sub>O nanocubes by tuning the substrate of ABTS at a fixed 4.84 mM H<sub>2</sub>O<sub>2</sub> (A), and tuning the H<sub>2</sub>O<sub>2</sub> concentration at a fixed 3.87 mM ABTS (B), respectively.

Compared with  $\text{Cu}_2\text{O}$ , the unique nanocage-shaped structure of  $\text{Fe}(\text{OH})_3$  nanocages can provide a higher BET surface area, leading to more catalytic active sites for  $\text{H}_2\text{O}_2$ , which was confirmed by the BET data (Figure 2B,C). Thus, the catalytic decomposition process of  $\text{H}_2\text{O}_2$  can be more effective and quicker. More importantly, Liu et al. demonstrated that the reduction reaction of  $\text{Fe}^{3+}/\text{Fe}^{2+}$  can effectively decompose  $\text{H}_2\text{O}_2$  to generate OH radicals and  $\text{O}_2^-$  radicals [12]. Both OH radicals and  $\text{O}_2^-$  radicals can rapidly oxidize the chromogenic substrate ABTS to form a vivid color, which can be easily recognized by the human eye. Subsequently,  $\text{Fe}(\text{OH})_3$  nanocages would have strong activity to convert  $\text{H}_2\text{O}_2$  into OH radicals and  $\text{H}_2\text{O}$  and thus exhibit excellent catalytic activity, which, in turn, results in a lower  $K_m$ .

The excellent peroxidase mimetic activity of the  $\text{Fe}(\text{OH})_3$  nanozyme was further verified by density functional theory (DFT). As depicted in Figure 5, it is defined that Fe (II) bounded with one water molecule as the zero potential start point ( $\text{R}_1$ ). When water molecule is replaced by hydrogen peroxide ( $\text{P}_1$ ), two both oxygen atoms are close to ferrous atom (0.208 nm). When Fe (II) turned to Fe (III) ( $\text{P}_2$ ), the bond length of Fe-O is 0.205 nm. Furthermore, another oxygen deviates from ferrous atom. The bond length of O-O in  $\text{H}_2\text{O}_2$  is elongated to 0.143 nm and dihedral angle increases from  $91.6^\circ$  to  $99.7^\circ$ . Therefore, it can be found that when iron is oxidized from II to III,  $\text{H}_2\text{O}_2$  begins to decompose into  $\cdot\text{OH}$  radicals and  $\text{H}_2\text{O}$ . It can be demonstrated that  $\text{Fe}(\text{OH})_3$  nanozyme is easier to catalyze  $\text{H}_2\text{O}_2$  to produce OH radical from the marked decline of the reaction system energy. Hydroxyl bounded to ferrous atom ( $\text{P}_3$ ) reacts with  $\text{H}_2\text{O}_2$ , producing water and  $\text{HO}_2$  radical ( $\text{P}_4$ ). Finally,  $\cdot\text{OH}$  radicals can react with another  $\text{H}_2\text{O}_2$  and detaches from  $\text{P}_4$ , while the transition state (TS) was found by searching the reaction. Ultimately, the site is available for water and  $\text{R}_1$  is recycled. Hydrogen atom is captured by OH radicals, so the O-H bond length is extended from 0.099 nm to 0.112 nm and the O-O bond length is shortened. By calculating energies of every stage,  $\text{H}_2\text{O}_2$  decomposition with the  $\text{Fe}(\text{OH})_3$  nanozyme easily takes place, indicating that the theoretical results are consisted with the Lineweaver–Burk plot.



**Figure 5.**  $\text{Fe}(\text{OH})_3$  catalyst reaction mechanism and energy change (insets are the structure of relevant molecules (ions); the center is iron ion, purple is ghost atom, red is oxygen atom, and white is hydrogen atom).

### 3.3. Characterization of the $\text{Fe}(\text{OH})_3@Ab_2$ Bioconjugate

The aminated  $\text{Fe}(\text{OH})_3$  nanocages were further studied in Figure S3 by a Fourier Infrared Spectrometer (FTIR). The obvious bands at  $584$  and  $3346\text{ cm}^{-1}$  were from Fe-O and O-H stretching vibrations in  $\text{Fe}(\text{OH})_3$ , respectively. The other two characteristic bands at  $952$  and  $1046\text{ cm}^{-1}$  were assigned to the N-H deformation vibration and C-NH<sub>2</sub> stretching vibration, respectively. Additionally, the deformation and stretching vibrations of C-H were distributed at  $1410$  and  $2936\text{ cm}^{-1}$ , respectively. Consequently, the UV-vis was further employed to investigate the formation of  $\text{Fe}(\text{OH})_3@Ab_2$ . As depicted from Figure 2G, the

characteristic absorption of protein only can be found in  $\text{Fe}(\text{OH})_3@Ab_2$  [30], demonstrating that the  $\text{Fe}(\text{OH})_3$  nanocages were successfully modified by  $Ab_2$ .

#### 3.4. The Feasibility of the $\text{Fe}(\text{OH})_3$ Nanocages-Induced Immunoassay

The fabrication of the  $\text{Fe}(\text{OH})_3$  nanocages-induced immunoassay was illustrated in Scheme 1. Briefly, the coated antigen and different concentrations of OTA could competitively bind to the certain amount of  $Ab_1$  in the 96-well plates. Subsequently, the  $Ab_1$  can specifically bind with  $\text{Fe}(\text{OH})_3@Ab_2$ , which can rapidly quench the fluorescence of 4-CN. Significantly, the fluorescence quenching effect may be attributed to the oxidation of 4-CN caused by the valence transition of the ferric ion in  $\text{Fe}(\text{OH})_3$  nanocages [41,42]. Subsequently, the uncombined  $\text{Fe}(\text{OH})_3@Ab_2$  was collected for the colorimetric detection, where the  $\text{Fe}(\text{OH})_3$  can catalyze the oxidation of ABTS to generate a vivid color change and UV-vis absorption intensity variation. Based on the mechanism of the designed self-tuning sensor, a trade-off was developed between the colorimetric and fluorescence signal, as one falls, the other is rising. It bears a striking resemblance to the balance of the two opposing principles in nature from the Book of Changes. Additionally, the signal acquisition of the fluorescence and colorimetric immunosensor was separated, and the detection results did not interfere with each other. Thus, the accuracy and reliability of the self-tuning immunosensor can be significantly enhanced.

Subsequently, in order to further demonstrate the feasibility of the designed platform, the controlled experiment of the developed self-tuning fluorescence and colorimetric immunosensor was performed. As indicated from Figure S4 in the Supporting Information, as for the fluorescence signal, the fluorescence peak of 4-CN at 377 nm has no obvious change as the time prolonged (Figure S4A, curves a and b). However, when  $\text{Fe}(\text{OH})_3$  nanocages were added to the reaction system, the fluorescence emission peak of 4-CN decreased significantly (Figure S4A, curve c), demonstrating that the  $\text{Fe}(\text{OH})_3$ -induced reaction can efficiently reduce the fluorescence intensity of 4-CN. Thus, the fluorescence signaling mechanism can be used for the sensitive and rapid detection of the target. For the colorimetric detection, when ABTS and  $\text{H}_2\text{O}_2$  were in solution, the color of the reaction system has no significant change (inset in Figure S4B, curves a and b). As shown in Figure S4B, only when the  $\text{Fe}(\text{OH})_3$  nanocages were added, the typical absorption spectrum of substrate ABTS can be found at 415 nm, exhibiting that  $\text{Fe}(\text{OH})_3$  nanocages can effectively catalyze the chromogenic substrate to form a vivid color change (inset in Figure S4B, curve c). This colorimetric platform can be highlighted by its naked eye readout without complicated instruments. To summarize, the designed self-tuning immunosensor is reasonable and practicable enough to achieve the desired detection performance; furthermore, it is even simple in manipulation and fabrication compared to traditional detection tools.

#### 3.5. Self-Tuning Colorimetric and Fluorescence Immunoassay of OTA

To achieve an optimum analytical performance, the relevant factors were optimized, such as the concentration of  $\text{H}_2\text{O}_2$ , reaction time, the excitation wavelength, and quenching time of 4-CN. Experimentally, the colorimetric detection performance was determined by investigating the absorbance change at characteristic 415 nm of the oxidized ABTS (oxABTS) product. The influence of  $\text{H}_2\text{O}_2$  concentration was shown in Figure S5A. As the  $\text{H}_2\text{O}_2$  concentration increased from 5 to 35 mM, the absorption peak at 415 nm of the system also enhanced remarkably. When the  $\text{H}_2\text{O}_2$  concentration was higher than 35 mM, the absorbance intensity of oxABTS did not increase remarkably. As seen from Figure S5B, the absorbance intensity of oxABTS also increased rapidly with the extension of reaction time, but after 3 min, it entered a relative steady phase. Therefore, the 35 mM of  $\text{H}_2\text{O}_2$  concentration and 3 min reaction time were selected for the subsequent experiments. Additionally, as in Figure S5C, it can be seen that the change of 4-CN fluorescence intensity reached an equilibrium at 4 min. Then, with the further extension of time, the reduction of 4-CN fluorescence intensity was not obvious. Hence, the optimal quenching time was set as 4 min for the following experiments.

Under the optimized conditions, the self-tuning immunosensor was constructed for OTA detection in light of colorimetric and fluorescence signals. As displayed in Figure 6A,B, when the OTA concentration increased, the UV-vis absorption intensity of the colorimetric signal increased while the quenching degree of 4-CN fluorescence intensity decreased. Concurrently, with the change in the OTA concentration, the immunosensor can generate a vivid color change that could be preliminarily identified by the naked eye (inset in Figure 6B). Simultaneously, the UV-vis absorption intensity and fluorescence intensity changes exhibited a good linear relation in the range of OTA concentrations between 1 ng/L and 5  $\mu\text{g/L}$  with a detection limit (0.68 ng/L, S/N = 3) (Figure 6C,D), where the regression equations were  $\text{Abs}_{415} = 1.7 + 0.4[\lg C_{\text{OTA}} (\mu\text{g/L})]$  ( $R^2 = 0.995$ , colorimetric signal) and  $\Delta I_{377\text{nm}} (\text{a.u.}) = 725.7 - 853.6[\lg C_{\text{OTA}} (\mu\text{g/L})]$  ( $R^2 = 0.986$ , fluorescence signal), respectively. Additionally, compared with other peroxidase or current OTA detection methods (Table S1), the designed self-tuning strategy based on the  $\text{Fe}(\text{OH})_3$  nanozyme had equivalent or better performance in the linear range or detection limit. Therefore, the significant self-calibration capability of this self-tuning detection platform can provide a more sensitive and accurate performance, particularly in OTA detection of actual samples.

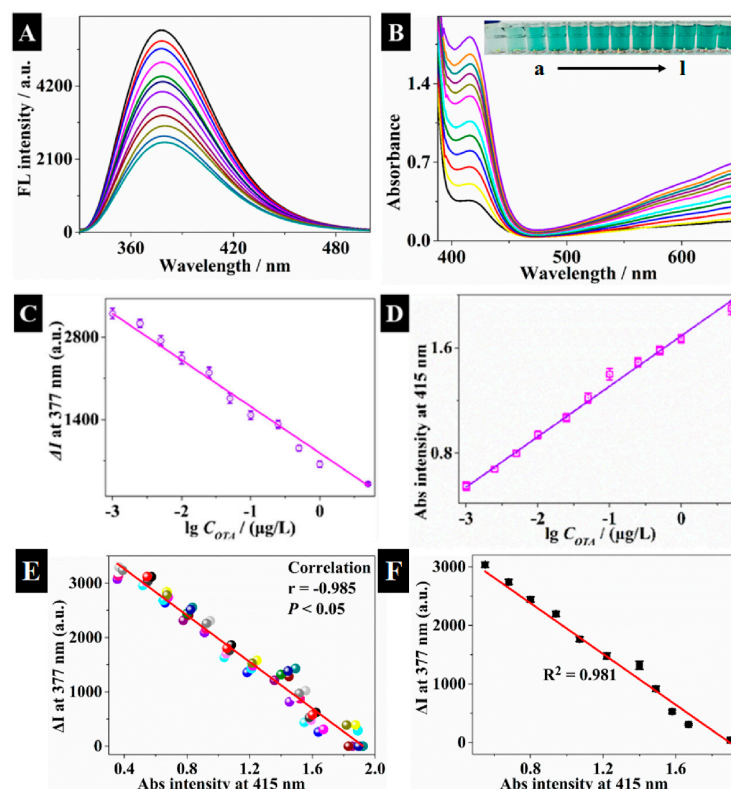


**Figure 6.** Fluorescence spectra (A) and UV-vis spectra (B) for different concentrations of OTA, (a) 0, (b) 0.001, (c) 0.0025, (d) 0.005, (e) 0.01, (f) 0.025, (g) 0.05, (h) 0.1, (i) 0.25, (j) 0.5, (k) 1, and (l) 5  $\mu\text{g/L}$  (from bottom to top in A and B correspond to a–l, respectively). Inset in B was the photographs of the colorimetric method at different concentrations of OTA. (C,D) Calibration curve based on the fluorescence spectra (A) and UV-vis spectra (B), respectively. (E,F) Pearson correlation analysis of the self-tuning immunosensor (E) and corresponding calibration curve (F).

To further demonstrate the substantial capability of the proposed self-tuning dual-mode immunosensor, the Pearson's correlation coefficient test was conducted to verify the correlation between fluorescence ( $\Delta I$ , the quenching level of fluorescence intensity at 377 nm) and colorimetric ( $\text{Abs}_{415}$ , the UV-vis absorbance intensity at 415 nm) signals ( $p < 0.05$  was regarded as significant difference). The results were summarized in Figure 6E, where a negative correlation was disclosed between  $\Delta I$  and  $\text{Abs}_{415}$  with a Pearson's correlation coefficient of  $-0.985$  ( $p < 0.05$ ). Concurrently, as reflected from

Figure 6F, the  $Abs_{415}$  of the colorimetric detection showed a good linear relationship with  $\Delta I$  changes of the fluorescence detection in the range of OTA concentration between 1 ng/L and 5  $\mu\text{g/L}$ , while the linear fitting equation was  $\Delta I = -4116.4 + 2170.5[Abs_{415\text{nm}} \text{ (a.u.)}]$  ( $R^2 = 0.981$ ). The statistical analysis further demonstrated that the two signals of the proposed self-tuning immunosensor can be mutually corrected, which substantially enhanced the accuracy and reliability of the detection results.

As for the actual application, an immunosensor should be not only sensitive but also stable and reproducible. Hence, to investigate the stability of the proposed sensor, as depicted in Figure 7A,B, the long-term stability of the strategy was evaluated with the same immunosensor using five OTA concentrations. After a week of storage, the fabricated sensor can retain sufficient stability for the detection of OTA. Subsequently, the reproducibility of the strategy was also demonstrated by employing five independent immunosensors with the same concentration of OTA (Figure 7C,D). As for colorimetric or fluorescence detection, there is basically no difference between five sensors, which demonstrated that the designed self-tuning immunosensor exhibited desirable stability and reproducibility for OTA detection.

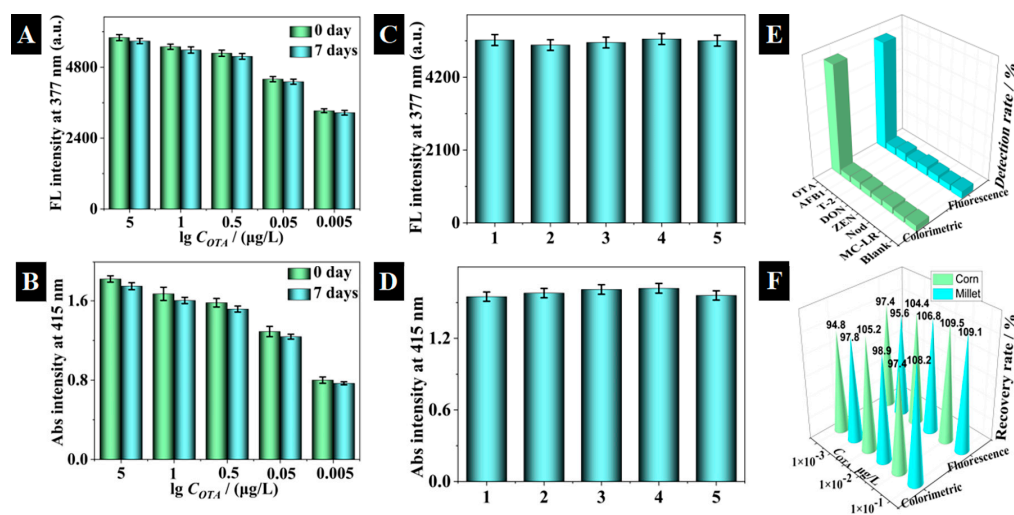


**Figure 7.** The stability (A,B) and reproducibility (C,D) of the self-tuning immunosensor, (E) selectivity of the self-tuning dual-modal immunosensor, and (F) the recoveries of the OTA detection in corn and millet samples.

Additionally, the interference investigation was conducted using microcystin-LR (MC-LR), nodularin (Nod), aflatoxin B<sub>1</sub> (AFB<sub>1</sub>), zearalenone (ZEN), deoxynivalenol (DON), and trichothecenes 2 (T-2). As seen in Figure 7E, the interferents had no significant influence on the self-tuning strategy for the OTA detection (both the colorimetric and fluorescence immunoassay), indicating the presented self-tuning immunosensor had excellent specificity to the target detection. Subsequently, in order to demonstrate the analytical reliability of the immunosensor and further investigate its potential practical application. Thus, the standard addition experiments were conducted by spiking the actual corn and millet samples at different concentrations of OTA standard solution (0.001, 0.01, and 0.1  $\mu\text{g/L}$ ). As depicted in Figure 7F, the recoveries of the self-tuning immunosensor were in a preferable range of 94.8–108.2% (colorimetric sensor) and 95.6–109.5% (fluorescence sensor), respectively. Hence, the developed self-tuning strategy has a promising performance for OTA detection in application.

#### 4. Conclusions

In this work, a coordinating etching facile strategy was proposed to synthesize  $\text{Fe}(\text{OH})_3$  nanocages by employing  $\text{Cu}_2\text{O}$  nanocubes as the sacrificial templates. It was demonstrated that  $\text{Fe}(\text{OH})_3$  nanocages resulted in the enhanced catalytic activity and followed the Lineweaver–Burk plot and Michaelis–Menten equation for the enzyme-catalyzed

ABTS/H<sub>2</sub>O<sub>2</sub> reaction. The enhanced peroxidase-like activity was mainly due to the large surface of the Fe(OH)<sub>3</sub> nanocages and the decrease in the reaction system energy, which was confirmed by the BET surface area and density functional theory. Subsequently, based on the high peroxidase-like activity of the Fe(OH)<sub>3</sub> nanocages, a self-tuning colorimetric and fluorescence strategy was designed for OTA detection. Due to the see-saw effect of signal modes, the two signals can be verified by each other directly to enhance the detection accuracy. Hence, OTA can be detected at a lower concentration of 0.68 ng/L, and the immunosensor showed excellent recovery rates of 94.8–109.5% in corn and millet samples with acceptable reproducibility and stability. In summary, this work not only investigates the feasibility of coordination etching for the synthesis of nanozymes with excellent peroxidase catalytic activity, but also broadens the detection platform for complex mycotoxin samples.

**Supplementary Materials:** The following supporting information can be downloaded at: <https://www.mdpi.com/article/10.3390/bios13060665/s1>, Figure S1: N<sub>2</sub> absorption–desorption isotherm of Cu<sub>2</sub>O nanocubes; Figure S2: (A) SEM image, (B) TEM image, (C) EDS, (D) elemental mappings of Cu<sub>2</sub>O nanocubes; Figure S3: FTIR spectrum of Fe(OH)<sub>3</sub>-NH<sub>2</sub> (inset illustration is russet color of the Fe(OH)<sub>3</sub> nanocages); Figure S4: Feasibility control experiments of the designed self-tuning fluorescence (A, a and b were 4-CN with the reaction times of 0 and 4 min, respectively; c was the mixture of 4-CN with Fe(OH)<sub>3</sub> with the time at 4 min) and colorimetric immunosensor (B, a: HAc-NaAc buffer (pH = 4.5)+ ABTS; b: HAc-NaAc buffer (pH = 4.5) + ABTS + H<sub>2</sub>O<sub>2</sub>; c: HAc-NaAc buffer (pH = 4.5) + ABTS + H<sub>2</sub>O<sub>2</sub> + Fe(OH)<sub>3</sub>, respectively); Figure S5: Effect of the concentration of H<sub>2</sub>O<sub>2</sub> (A) and the reaction time (B) on the colorimetric part. Effect of the quenching time of 4-CN (C) on the fluorescence part; Table S1: Comparison with other peroxidase or current OTA detection methods [43–54].

**Author Contributions:** Conceptualization, H.Z., Y.L.; methodology, H.Z., B.W., Y.L.; formal analysis, H.Z., B.W. and Y.L.; investigation, H.Z., B.W. and Y.L.; writing—original draft preparation, H.Z., B.W.; writing—review and editing, Y.L.; supervision, Y.L. All authors have read and agreed to the published version of the manuscript.

**Funding:** This work was supported by the Educational Commission Foundation of Guangdong Province (2020ZDZX2025), Guangdong Basic and Applied Basic Research Foundation (2021A1515010208), the China Postdoctoral Science Foundation (2022M711058), Natural Science Foundation of Henan Province (232300420195), and the talent foundation of Henan Agricultural University (30501354).

**Institutional Review Board Statement:** Not applicable.

**Informed Consent Statement:** Not applicable.

**Data Availability Statement:** The data presented in this study are available on request from the corresponding author.

**Conflicts of Interest:** There is no conflict of interest.

## References

1. Weng, G.; Shen, X.; Li, J.; Wang, J.; Zhu, J.; Zhao, J. A plasmonic ELISA for multi-colorimetric sensing of C-reactive protein by using shell dependent etching of Ag coated Au nanopyramids. *Anal. Chim. Acta* **2022**, *1221*, 340129. [[CrossRef](#)] [[PubMed](#)]
2. Li, G.; Liu, S.; Huo, Y.; Zhou, H.; Li, S.; Lin, X.; Kang, W.; Li, S.; Gao, Z. “Three-in-one” nanohybrids as synergistic nanozymes assisted with exonuclease I amplification to enhance colorimetric aptasensor for ultrasensitive detection of kanamycin. *Anal. Chim. Acta* **2022**, *1222*, 340178. [[CrossRef](#)] [[PubMed](#)]
3. Yang, S.; Du, J.; Wei, M.; Huang, Y.; Zhang, Y.; Wang, Y.; Li, J.; Wei, W.; Qiao, Y.; Dong, H.; et al. Colorimetric-photothermal-magnetic three-in-one lateral flow immunoassay for two formats of biogenic amines sensitive and reliable quantification. *Anal. Chim. Acta* **2022**, *1239*, 340660. [[CrossRef](#)] [[PubMed](#)]
4. Li, Y.; Qian, Z.; Shen, C.; Gao, Z.; Tang, K.; Liu, Z.; Chen, Z. Colorimetric sensors for alkaloids based on the etching of Au@MnO<sub>2</sub> nanoparticles and MnO<sub>2</sub> nanostars. *ACS Appl. Nano Mater.* **2021**, *4*, 8465–8472. [[CrossRef](#)]
5. He, Y.; Tian, F.; Zhou, J.; Zhao, Q.; Fu, R.; Jiao, B. Colorimetric aptasensor for ochratoxin A detection based on enzyme induced gold nanoparticle aggregation. *J. Hazard. Mater.* **2020**, *1132*, 101–109. [[CrossRef](#)]
6. Wang, D.; Zhang, F.; Prabhakar, A.; Qin, X.; Forzani, E.; Tao, N. Colorimetric sensor for online accurate detection of breath acetone. *ACS Sens.* **2020**, *6*, 450–453. [[CrossRef](#)]

7. Mustafa, F.; Andreescu, S. Paper-based enzyme biosensor for one-step detection of hypoxanthine in fresh and degraded fish. *ACS Sens.* **2020**, *5*, 4092–4100. [[CrossRef](#)]
8. Moon, J.; Kwon, H.; Yong, D.; Lee, I.C.; Kim, H.; Kang, H.; Lim, E.; Lee, K.; Jung, J.; Park, H.; et al. Colorimetric detection of SARS-CoV-2 and drug-resistant pH1N1 using CRISPR/dCas9. *ACS Sens.* **2020**, *5*, 4017–4026. [[CrossRef](#)]
9. Xu, S.; Jiang, L.; Liu, Y.; Liu, P.; Wang, W.; Luo, X. A morphology-based ultrasensitive multicolor colorimetric assay for detection of blood glucose by enzymatic etching of plasmonic gold nanobipyramids. *Anal. Chim. Acta* **2019**, *1071*, 53–58. [[CrossRef](#)]
10. Imran, M.; Chen, M. Self-sensitized and reversible O<sub>2</sub> reactivity with bisphenalenyls for simple, tunable, and multicycle colorimetric oxygen-sensing films. *ACS Appl. Mater. Interfaces* **2022**, *14*, 1817–1825. [[CrossRef](#)]
11. Ding, L.; Shao, X.; Wang, M.; Zhan, H.; Lu, L. Dual-mode immunoassay for diethylstilbestrol based on peroxidase activity and photothermal effect of black phosphorus-gold nanoparticle nanohybrids. *Anal. Chim. Acta* **2022**, *1187*, 339171. [[CrossRef](#)] [[PubMed](#)]
12. Zhu, H.; Cai, Y.; Qileng, A.; Quan, Z.; Zeng, W.; He, K.; Liu, Y. Template-assisted Cu<sub>2</sub>O@Fe(OH)<sub>3</sub> yolk-shell nanocages as biomimetic peroxidase: A multi-colorimetry and ratiometric fluorescence separated-type immunosensor for the detection of ochratoxin A. *J. Hazard. Mater.* **2021**, *411*, 125090. [[CrossRef](#)] [[PubMed](#)]
13. Li, L.; Liu, X.; Zhu, R.; Wang, B.; Yang, J.; Xu, F.; Ramaswamy, S.; Zhang, X. Fe<sup>3+</sup>-doped aminated lignin as peroxidase-mimicking nanozymes for rapid and durable colorimetric detection of H<sub>2</sub>O<sub>2</sub>. *ACS Sustain. Chem. Eng.* **2021**, *9*, 12833–12843. [[CrossRef](#)]
14. Feng, E.; Zheng, T.; Tian, Y. Dual-mode Au nanoprobe based on surface enhancement raman scattering and colorimetry for sensitive determination of telomerase activity both in cell extracts and the urine of patients. *ACS Sens.* **2019**, *4*, 211–217. [[CrossRef](#)] [[PubMed](#)]
15. Wei, J.; Chen, H.M.; Chen, H.; Cui, Y.; Qileng, A.; Qin, W.; Liu, W.; Liu, Y. Multifunctional peroxidase-encapsulated nanoliposomes: Bioetching-induced photoelectrometric and colorimetric immunoassay for broad-spectrum detection of ochratoxins. *ACS Appl. Mater. Interfaces* **2019**, *11*, 23832–23839. [[CrossRef](#)] [[PubMed](#)]
16. Cai, Y.; Zhu, H.; Zhou, W.; Qiu, Z.; Chen, C.; Qileng, A.; Li, K.; Liu, Y. Capsulation of AuNCs with AIE effect into metal-organic framework for the marriage of fluorescence and colorimetric biosensor to detect organophosphorus pesticides. *Anal. Chem.* **2021**, *93*, 7275–7282. [[CrossRef](#)]
17. Wei, J.; Chang, W.; Qileng, A.; Liu, W.; Zhang, Y.; Rong, S.; Lei, H.; Liu, Y. Dual-modal split-type immunosensor for sensitive detection of microcystin-LR: Enzyme-induced photoelectrochemistry and colorimetry. *Anal. Chem.* **2018**, *90*, 9606–9613. [[CrossRef](#)]
18. Li, D.; Li, N.; Zhao, L.; Xu, S.; Sun, Y.; Ma, P.; Song, D.; Wang, X. Colorimetric and fluorescent dual-mode measurement of blood glucose by organic silicon nanodots. *ACS Appl. Nano. Mater.* **2020**, *3*, 11600–11607. [[CrossRef](#)]
19. Guo, Z.; Jia, Y.; Song, X.; Lu, J.; Lu, X.; Liu, B.; Han, J.; Huang, Y.; Zhang, J.; Chen, T. Giant gold nanowire vesicle-based colorimetric and SERS dual-mode immunosensor for ultrasensitive detection of vibrio parahemolyticus. *Anal. Chem.* **2018**, *90*, 6124–6130. [[CrossRef](#)]
20. Wei, H.; Wang, E. Nanomaterials with enzyme-like characteristics (nanozymes): Next-generation artificial enzymes. *Chem. Soc. Rev.* **2013**, *42*, 6060–6093. [[CrossRef](#)]
21. Li, J.; Lu, N.; Han, S.; Li, X.; Wang, M.; Cai, M.; Tang, Z.; Zhang, M. Construction of bio-nano interfaces on nanozymes for bioanalysis. *ACS Appl. Mater. Interfaces* **2021**, *13*, 21040–21050. [[CrossRef](#)] [[PubMed](#)]
22. Zhang, J.; Wu, S.; Lu, X.; Wu, P.; Liu, J. Manganese as a catalytic mediator for photo-oxidation and breaking the pH limitation of nanozymes. *Nano Lett.* **2019**, *19*, 3214–3220. [[CrossRef](#)] [[PubMed](#)]
23. Gao, L.; Zhuang, J.; Nie, L.; Zhang, J.; Zhang, Y.; Gu, N.; Wang, T.; Feng, J.; Yang, D.; Perrett, S.; et al. Intrinsic peroxidase-like activity of ferromagnetic nanoparticles. *Nat. Nanotechnol.* **2007**, *2*, 577–583. [[CrossRef](#)]
24. Chen, Q.; Zhang, X.; Li, S.; Tan, J.; Xu, C.; Huang, Y. MOF-derived Co<sub>3</sub>O<sub>4</sub>@Co-Fe oxide double-shelled nanocages as multi-functional specific peroxidase-like nanozyme catalysts for chemo/biosensing and dye degradation. *Chem. Eng. J.* **2020**, *395*, 125130. [[CrossRef](#)]
25. Mu, J.; Zhang, L.; Zhao, M.; Wang, Y. Catalase mimic property of Co<sub>3</sub>O<sub>4</sub> nanomaterials with different morphology and its application as a calcium sensor. *ACS Appl. Mater. Interfaces* **2014**, *6*, 7090–7098. [[CrossRef](#)] [[PubMed](#)]
26. Jin, C.; Lian, J.; Gao, Y.; Guo, K.; Wu, K.; Guo, L.; Zhang, X.X.; Zhang, X.; Liu, Q.Y. Si doped CoO nanorods as peroxidase mimics for colorimetric sensing of reduced glutathione. *ACS Sustainable Chem. Eng.* **2019**, *7*, 13989–13998. [[CrossRef](#)]
27. Chen, Y.; Ji, Y.; Shen, T. Reduced graphene oxide-supported hollow Co<sub>3</sub>O<sub>4</sub>@N-doped porous carbon as peroxydisulfate activator for sulfamethoxazole degradation. *Chem. Eng. J.* **2022**, *430*, 132951. [[CrossRef](#)]
28. Liu, P.; Zhao, M.; Zhu, H.; Zhang, M.; Li, X.; Wang, M.; Liu, B.; Pan, J.; Niu, X. Dual-mode fluorescence and colorimetric detection of pesticides realized by integrating stimulus-responsive luminescence with oxidase-mimetic activity into cerium-based coordination polymer nanoparticles. *J. Hazard. Mater.* **2022**, *423*, 127077. [[CrossRef](#)]
29. Zheng, H.; Zeng, Y.; Chen, J.; Lin, R.; Zhuang, W.; Cao, R.; Lin, Z. Zr-based metal organic frameworks with intrinsic peroxidase-like activity for ultradeep oxidative desulfurization: Mechanism of H<sub>2</sub>O<sub>2</sub> decomposition. *Inorg. Chem.* **2019**, *58*, 6983–6992. [[CrossRef](#)]
30. Li, Z.; Ni, P.; Zhang, C.; Wang, B.; Duan, G.; Chen, C.; Jiang, Y.; Lu, Y. Carbon dots confined in N-doped carbon as peroxidase-like nanozyme for detection of gastric cancer relevant D-amino acids. *Chem. Eng. J.* **2022**, *428*, 131396. [[CrossRef](#)]
31. Tang, L.; Li, J. Plasmon-based colorimetric nanosensors for ultrasensitive molecular diagnostics. *ACS Sens.* **2017**, *2*, 857–875. [[CrossRef](#)] [[PubMed](#)]

32. Huang, X.; Wu, S.; Hu, H.; Sun, J. Au nanostar@4-MBA@Au core-shell nanostructure coupled with exonuclease III-assisted cycling amplification for ultrasensitive SERS detection of ochratoxin A. *ACS Sens.* **2020**, *5*, 2636–2643. [[CrossRef](#)]
33. Suea-Ngam, A.; Howes, P.D.; Stanley, C.E.; Demello, A.J. An exonuclease I-assisted silver-metallized electrochemical aptasensor for ochratoxin A detection. *ACS Sens.* **2019**, *4*, 1560–1568. [[CrossRef](#)] [[PubMed](#)]
34. Zhang, D.; Zhang, H.; Guo, L.; Zheng, K.; Han, X.; Zhang, Z. Delicate control of crystallographic facet-oriented Cu<sub>2</sub>O nanocrystals and the correlated adsorption ability. *J. Mater. Chem.* **2009**, *19*, 5220–5225. [[CrossRef](#)]
35. Walker, M.; Harvey, A.J.; Sen, A.; Dessent, C.E. Performance of M06, M06-2X, and M06-HF density functionals for conformationally flexible anionic clusters: M06 functionals perform better than B3LYP for a model system with dispersion and ionic hydrogen-bonding interactions. *J. Phys. Chem. C* **2013**, *117*, 12590–12600. [[CrossRef](#)] [[PubMed](#)]
36. Chiodo, S.; Russo, N.; Sicilia, E. LANL2DZ basis sets recontracted in the framework of density functional theory. *J. Chem. Phys.* **2006**, *125*, 104107. [[CrossRef](#)]
37. Tsuneda, T.; Taketsugu, T. Theoretical investigations on hydrogen peroxide decomposition in aquo. *Phys. Chem. Chem. Phys.* **2018**, *38*, 1–24. [[CrossRef](#)]
38. Nai, J.; Tian, Y.; Guan, X.; Guo, L. Pearson's principle inspired generalized strategy for the fabrication of metal hydroxide and oxide nanocages. *J. Am. Chem. Soc.* **2013**, *135*, 16082–16091. [[CrossRef](#)] [[PubMed](#)]
39. Biesinger, M.C.; Payne, B.P.; Grosvenor, A.P.; Lau, L.; Gerson, A.R.; Smart, R. Resolving surface chemical states in XPS analysis of first row transition metals, oxides and hydroxides: Cr, Mn, Fe, Co and Ni. *Appl. Surf. Sci.* **2011**, *257*, 2717–2730. [[CrossRef](#)]
40. Xue, T.; Jiang, S.; Qu, Y.; Su, Q.; Cheng, R.; Dubin, S.; Chiu, C.; Kaner, R.; Huang, Y.; Duan, X. Graphene-supported hemin as a highly active biomimetic oxidation catalyst. *Angew. Chem. Int. Ed.* **2012**, *51*, 3822–3825. [[CrossRef](#)]
41. He, Y.; Lv, Y.; Hu, J.; Qi, L.; Hou, X. Simple, sensitive and on-line fluorescence monitoring of photodegradation of phenol and 2-naphthol. *Luminescence* **2007**, *22*, 309–316. [[CrossRef](#)] [[PubMed](#)]
42. Sayour, H.E.M.; Razek, T.M.A.; Fadel, K.F. Flow injection spectrofluorimetric determination of iron in industrial effluents based on fluorescence quenching of 1-naphthol-2-sulfonate. *J. Fluoresc.* **2011**, *21*, 1385–1391. [[CrossRef](#)] [[PubMed](#)]
43. Chen, J.; Wei, Q.; Yang, L.; Li, J.; Lu, T.; Liu, Z.; Zhong, G.; Weng, X.; Xu, X. Multimodal ochratoxin A-aptasensor using 3'-FAM-enhanced exonuclease I tool and magnetic microbead carrier. *Anal. Chem.* **2022**, *94*, 10921–10929. [[CrossRef](#)] [[PubMed](#)]
44. Wu, S.; Liu, L.; Duan, N.; Wang, W.; Yu, Q.; Wang, Z. A test strip for ochratoxin A based on the use of aptamer-modified fluorescence upconversion nanoparticles. *Mirochim. Acta* **2018**, *185*, 497. [[CrossRef](#)]
45. Hao, L.; Chen, J.; Chen, X.; Ma, T.; Cai, X.; Duan, H.; Leng, Y.; Huang, X.; Xiong, Y. A novel magneto-gold nanohybrid-enhanced lateral flow immunoassay for ultrasensitive and rapid detection of ochratoxin A in grape juice. *Food Chem.* **2021**, *336*, 127710. [[CrossRef](#)]
46. Lv, L.; Li, D.; Cui, C.; Zhao, Y.; Guo, Z. Nuclease-aided target recycling signal amplification strategy for ochratoxin A monitoring. *Biosens. Bioelectron.* **2017**, *87*, 136–141. [[CrossRef](#)]
47. Wang, C.; Tan, R.; Chen, D. Fluorescence method for quickly detecting ochratoxin A in flour and beer using nitrogen doped carbon dots and silver nanoparticles. *Talanta* **2018**, *182*, 363–370. [[CrossRef](#)]
48. Pacheco, J.; Castro, M.; Machado, S.; Barroso, M.F.; Nouws, H.P.A.; Delerue-Matos, C. Molecularly imprinted electrochemical sensor for ochratoxin A detection in food samples. *Sensor. Actuat. B: Chem.* **2015**, *215*, 107–112. [[CrossRef](#)]
49. Hu, S.; Ouyang, W.; Guo, L.; Lin, Z.; Jiang, X.; Qiu, B.; Chen, G. Facile synthesis of Fe<sub>3</sub>O<sub>4</sub>/g-C<sub>3</sub>N<sub>4</sub>/HKUST-1 composites as a novel biosensor platform for ochratoxin A. *Biosens. Bioelectron.* **2017**, *92*, 718–723. [[CrossRef](#)]
50. Zeng, H.L.; Ma, L.; Xia, X.H. G-quadruplex specific dye-based ratiometric FRET aptasensor for robust and ultrafast detection of toxin. *Dyes Pigm.* **2019**, *164*, 35–42. [[CrossRef](#)]
51. Zhang, X.; Zhi, H.; Zhu, M.; Wang, F. Electrochemical/visual dual-readout aptasensor for ochratoxin A detection integrated into a miniaturized paper-based analytical device. *Biosens. Bioelectron.* **2021**, *180*, 113146. [[CrossRef](#)] [[PubMed](#)]
52. Li, X.; Chen, X.; Huang, H. Development of a novel label-free impedimetric electrochemical sensor based on hydrogel/chitosan for the detection of ochratoxin A. *Talanta* **2021**, *226*, 122183. [[CrossRef](#)] [[PubMed](#)]
53. Wang, X.; Gong, M.; Jin, X.; Jiang, M.; Xu, J. A novel electrochemical sensor for ochratoxin A based on the hairpin aptamer and double report DNA via multiple signal amplification strategy. *Sensor Actuat. B-Chem.* **2019**, *281*, 595–601. [[CrossRef](#)]
54. Guo, J.; Pan, L.; Wang, M.; Chen, L.; Zhao, X. Exogenous interference and autofluorescence-free ratiometric aptasensor for detection of OTA based on dual-colored persistent luminescence nanoparticles. *Food Chem.* **2023**, *413*, 135611. [[CrossRef](#)] [[PubMed](#)]

**Disclaimer/Publisher's Note:** The statements, opinions and data contained in all publications are solely those of the individual author(s) and contributor(s) and not of MDPI and/or the editor(s). MDPI and/or the editor(s) disclaim responsibility for any injury to people or property resulting from any ideas, methods, instructions or products referred to in the content.